

A High-Performance Solution-Processed Organic Photodetector for Near-Infrared Sensing

Jianfei Huang, Jaewon Lee, Joachim Vollbrecht, Viktor V. Brus, Alana L. Dixon, David Xi Cao, Ziyue Zhu, Zhifang Du, Hengbin Wang, Kilwon Cho, Guillermo C. Bazan,* and Thuc-Quyen Nguyen*

Sensitive detection of near-infrared (NIR) light enables many important applications in both research and industry. Current organic photodetectors suffer from low NIR sensitivity typically due to early absorption cutoff, low responsivity, and/or large dark/noise current under bias. Herein, organic photodetectors based on a novel ultranarrow-bandgap nonfullerene acceptor, CO1-4Cl, are presented, showcasing a remarkable responsivity over 0.5 A W^{-1} in the NIR spectral region (920–960 nm), which is the highest among organic photodiodes. By effectively delaying the onset of the space charge limited current and suppressing the shunt leakage current, the optimized devices show a large specific detectivity around 10^{12} Jones for NIR spectral region up to 1010 nm, close to that of a commercial Si photodiode. The presented photodetectors can also be integrated in photoplethysmography for real-time heart-rate monitoring, suggesting its potential for practical applications.

Near-infrared (NIR) light usually corresponds to the region of electromagnetic radiation with wavelength spanning from about 750 to 1400 nm.^[1] Despite being invisible to human visual perception, NIR sensing finds applications in a variety of technologies, including medical monitoring,^[2] quality inspection,^[3] machine vision,^[4] and bioimaging.^[5] NIR sensing has been conventionally realized with detectors based on single-crystal inorganic semiconductor materials (e.g., Si, Ge, GaInAs), which

typically have drawbacks including costly processing, mechanical inflexibility, and sensitivity to temperature.^[6–8]

Owing to the low cost, solution processing, material tunability, unique structure–property relationships, and good mechanical flexibility, organic semiconductors emerged as an exciting candidate for integrated electronics, lighting, solar cells, and photodetection. Particularly, photodetectors based on organic semiconductors have witnessed increasing research endeavor, especially for extending their response from visible (vis) spectrum into the NIR spectrum, leading to novel organic photodetectors (OPDs) with improved NIR sensitivity and broadband activity within the past decade. A critical

prerequisite for fabricating OPDs with spectral response that extends into the NIR region is to incorporate a component with a sufficiently narrow optical bandgap ($E_g^{\text{opt}} < 1.55 \text{ eV}$), allowing exciton generation by the low-energy photons. Materials including narrow-bandgap conjugated polymers (e.g., CPDT-TQ,^[7] PTT,^[9] PDDTT,^[10] PDPP3T^[11]), organic salts,^[12] organic dyes,^[13] and metallo-organics,^[14,15] have been explored for this purpose and found success in achieving spectral response tailing off beyond 1000 nm. Nonetheless, the photo-detection performance is generally limited by the low external quantum efficiency (EQE) due to the poor carrier generation and extraction, large noise current, and the consequently low detectivity related to the poorly suppressed charge transport in the dark under reverse bias. In the pursuit of photon utilization in the NIR region, narrow-bandgap nonfullerene acceptors (NFAs) have recently achieved substantial success in organic bulk-heterojunction (BHJ) systems. For example, Yao et al. reported a small molecule, IEICO-4F, with E_g^{opt} of 1.24 eV, which demonstrated EQE greater than 60% at wavelengths larger than 800 nm for a BHJ solar cell.^[16] Lee et al. demonstrated an ultranarrow-bandgap ($E_g^{\text{opt}} = 1.1 \text{ eV}$) NFA with 50% of EQE at 1000 nm when combined with poly[4,8-bis(5-(2-ethylhexyl)thiophen-2-yl)benzo[1,2-b;4,5-b']dithiophene-2,6-diyl-*alt*-(4-(2-ethylhexyl)-3-fluorothieno[3,4-b]thiophene)-2-carboxylate-2-6-diyl)] (PTB7-Th).^[17] Although the NFAs are actively explored for organic solar cells, their application in highly NIR-sensitive broadband OPDs, especially with well-balanced photoresponse and electrical characteristics in the

J. Huang, Dr. J. Lee, Dr. J. Vollbrecht, Dr. V. V. Brus, A. L. Dixon, D. X. Cao, Z. Zhu, Z. Du, Prof. G. C. Bazan, Prof. T.-Q. Nguyen
Center for Polymers and Organic Solids
University of California
Santa Barbara, CA 93106, USA
E-mail: bazan@chem.ucsb.edu; quyen@chem.ucsb.edu

J. Huang, Dr. J. Lee, Z. Zhu, Dr. H. Wang, Prof. G. C. Bazan,
Prof. T.-Q. Nguyen
Mitsubishi Chemical Center for Advanced Materials
Materials Research Laboratory
University of California
Santa Barbara, CA 93106, USA
Prof. K. Cho
Center for Advanced Soft Electronics
Department of Chemical Engineering
Pohang University of Science and Technology
Pohang 37673, Republic of Korea

 The ORCID identification number(s) for the author(s) of this article can be found under <https://doi.org/10.1002/adma.201906027>.

DOI: 10.1002/adma.201906027

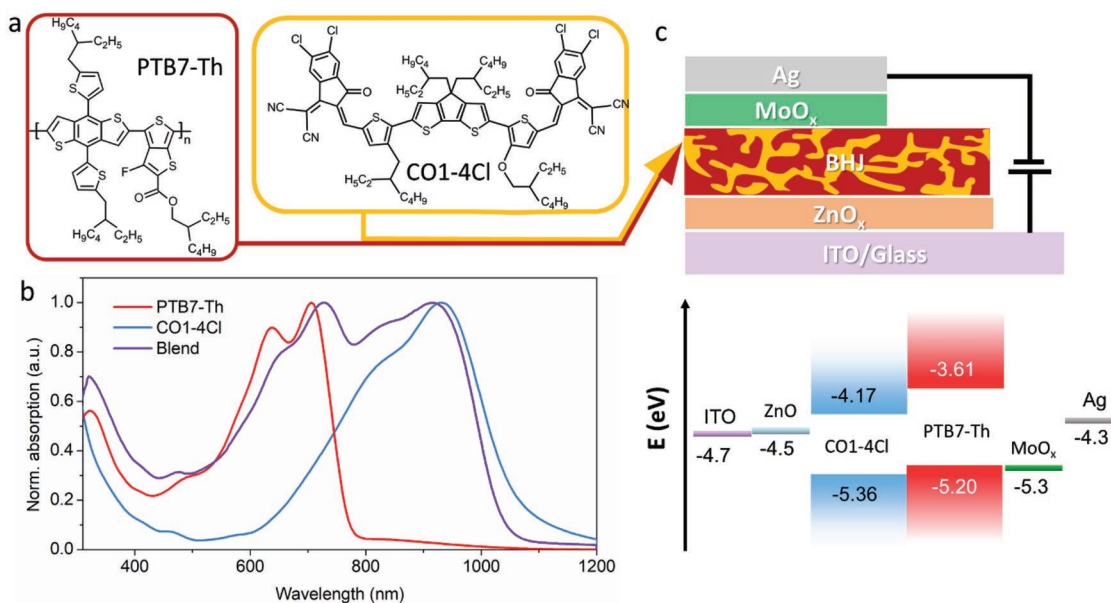


Figure 1. a) Chemical structures of the donor PTB7-Th and the acceptor CO1-4Cl. b) Normalized thin film absorption of the PTB7-Th (red), CO1-4Cl (blue), and their BHJ blend (purple). c) Device structure and energy diagram of the NIR OPD. The HOMO level is derived from the thin-film cyclic voltammogram. The LUMO is calculated by the following equation: $E_{(LUMO)} = E_g^{opt} + E_{(HOMO)}$.

dark remains comparatively underexplored.^[6,18] In addition to the improvable photoresponse, the large dark/noise current under reverse bias has been a crucial limiting factor to achieving high sensitivity for OPDs. Even with a high NIR EQE achieved at 70%, large noise signals can lead to an undermined detectivity below 10^{11} Jones.^[19] While the application of the bulk heterojunction concept has greatly boosted exciton dissociation and overall quantum efficiency of organic photodiodes, the drawback brought by this approach is one of the most challenging to tackle in photodetection. For BHJ organic photodiodes, both the donor and acceptor materials may have direct contact with the anode and cathode. Even with application of charge blocking layers, this scenario raises the possibility of injection of holes from the cathode to the highest occupied molecular orbital (HOMO) of the donor, and electrons from the anode to the lowest unoccupied molecular orbital (LUMO) of the acceptor under reverse bias, leading to a large undesirable dark/noise current depending on different noise mechanisms.^[19,20] This can be more severe with narrow-bandgap systems due to smaller injection barriers.^[21] Therefore, simultaneously achieving high NIR photoresponse and low dark/noise current with narrow-bandgap materials is fundamentally challenging.

Herein, we demonstrate solution-processed BHJ OPDs with outstanding vis-to-NIR sensing capability based on a novel NFA. By including the NFA with a narrow optical bandgap of ≈ 1.19 eV, large photoresponse can be extended up to 1100 nm. After optimization, the OPDs can provide a maximum NIR responsivity of ≈ 0.5 A W⁻¹ in the wavelength region of 920–940 nm, outmatching the majority of OPDs.^[6] To tackle the large dark/noise current commonly associated with BHJ OPDs, we have adopted a so-called “thick junction” strategy to suppress the shunt leakage and postpone the onset of space charge limited current.^[22] Benefiting from a well-balanced performance

under illumination and dark conditions, the presented OPDs give a low dark current density on the order of nanoamperes per centimeter square even at the moderate reverse bias of -2 V, leading to a peak shot-noise-limited detectivity over 10^{13} Jones. With a more careful evaluation of the noise current, a high detectivity over 10^{12} Jones can be confirmed from 580 nm (visible light) to 1010 nm (NIR), rendering these devices among the best high-performance broadband OPDs for vis-to-NIR photodetection.

The active layer of our OPDs contains a BHJ system that comprises a polymer donor (PTB7-Th) and a novel NFA, abbreviated as CO1-4Cl (see Figure 1a for the chemical structure). The general design of CO1-4Cl can be summarized by an A–D’–D–D’’–A asymmetrical configuration that is based on cyclopentadithiophene (CPDT) as the central donor (D) unit flanked with two different thienyl units as the subdonor (D’ and D’’) fragments, and is terminated by acceptor (A) units consisting of 2-(5,6-dichloro-3-oxo-2,3-dihydro-1H-inden-1-ylidene) malononitrile. CO1-4Cl was synthesized according to our previous work with slight modifications.^[23] The synthetic route and materials characterization are shown in Figures S1–S4 (Supporting Information). Strong NIR absorption can be observed from the absorption spectrum of the PTB7-Th:CO1-4Cl blend, peaking around 920 nm, which originates from the ultranarrow-bandgap acceptor material, CO1-4Cl (Figure 1b). The E_g^{opt} of CO1-4Cl is ≈ 1.19 eV according to the onset of absorption. The peak in the range of 700–800 nm corresponds to the absorption of PTB7-Th. The device structure and the corresponding energy diagram are provided in Figure 1c. The staggered bandgap alignment of CO1-4Cl and PTB7-Th demonstrates possibility of efficient charge separation following photogeneration of excitons. An inverted architecture was adopted for the fabrication of the OPDs. The zinc oxide layer, serving as a hole-blocking layer, and the BHJ active layer were consecutively solution-processed

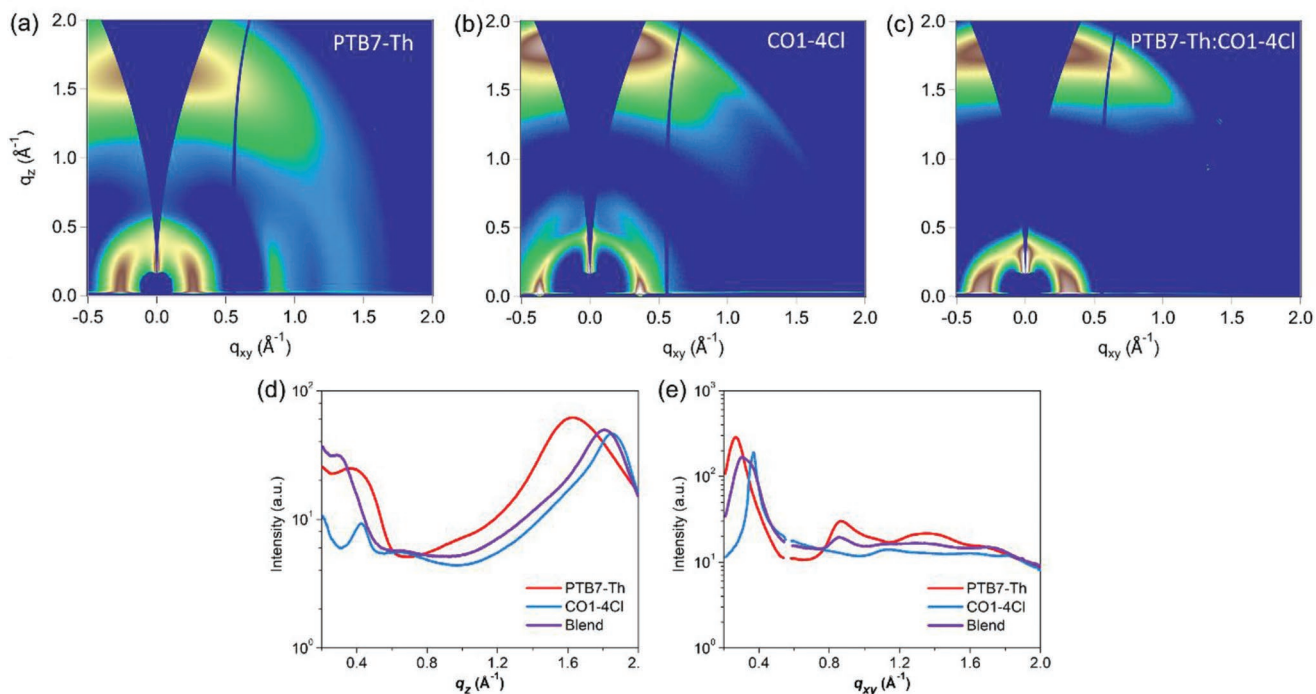


Figure 2. a–c) 2D GIWAXS images of the films of PTB7-Th, CO1-4Cl, and the blend. d,e) Out-of-plane and in-plane line-cut profiles for the neat and blend films.

onto a glass substrate coated with an indium tin oxide (ITO) layer, followed by the thermally evaporated electron-blocking layer of molybdenum oxide and silver top electrode. The thickness of the active layer was varied by adjusting the concentration of PTB7-Th:CO1-4Cl blend solutions, producing devices with two typical active layer thickness of ≈ 87 nm (the “thin” device) and ≈ 300 nm (the “thick” device). Atomic force microscopy (AFM) images (Figure S5, Supporting Information) indicate that the BHJ active layers of both thin and thick devices have similar surface morphologies except that the root-mean-square (rms) roughness is slightly larger for the thick device (4.475 nm) than the thin device (3.327 nm). Both rms thickness values are small relative to the total thickness of the active layer, being 1.49 and 3.82% of the total thickness for the thick and thin devices, respectively. This is beneficial for reducing shunt leakage related to local nonuniformity of interfaces.

Grazing-incidence wide-angle X-ray scattering (GIWAXS) was applied to study the molecular packing and crystalline feature of the neat films of the donor, acceptor, and their blend. 2D GIWAXS patterns and the line-cut profiles for out-of-plane and in-plane features are shown in **Figure 2**. A detailed summary of peak positions, stacking distance (d), and coherence lengths (L_c) are summarized in Table S1 (Supporting Information). The presence of intense scattering at a large q_z and small q_{xy} in both neat films (Figure 2a,b) indicates that both the donor and acceptor adopt face-on orientation in their neat films. PTB7-Th and CO1-4Cl exhibit π - π stacking distances of 0.39 nm ($1.63 q_z$) and 0.34 nm ($1.85 q_z$), respectively. CO1-4Cl shows greater crystallinity than PTB7-Th, as evidenced by the narrower peaks (Figure 2d,e), and better long-range order, as reflected by larger L_c values (Table S1, Supporting Information). The features

near $0.42 q_z$ for CO1-4Cl in the neat film may be assigned to the presence of edge-on crystallites. However, these scattering features are much less intense than those from the face-on crystallites, revealing CO1-4Cl predominantly adopts face-on orientation. For the BHJ blend, the π - π stacking of CO1-4Cl near $1.85 q_z$ is retained while the longer distance π - π stacking of CO1-4Cl and PTB7-Th near $1.64 q_z$ is not present. Instead, an additional π - π stacking peak is identified near $1.79 q_z$ which represents a new stacking distance ($d = 0.35$ nm) not seen in either component. This likely represents a new polymorph which cannot be assigned definitively to CO1-4Cl or PTB7-Th, but indicates a tighter π - π stacking of the materials. Noticeably, the weak edge-on scattering feature observed in neat CO1-4Cl film is hardly observable in the blend film, which indicates the further suppression of the minor edge-on character of CO1-4Cl when being codeposited with PTB7-Th.^[23] Overall, the combination of these donor and acceptor materials in BHJ blend leads to preferential face-on orientation and smaller π - π stacking distances, which are favorable for efficient charge transport in vertical photodetectors where photogenerated carriers are extracted in the direction normal to the substrate.

Figure 3a shows the semilog plot of the current–voltage (J - V) characteristics of the OPDs. Photodetectors based on vertical junction diodes typically work in the photoconductive mode, that is, under reverse bias. For detecting weak optical signals or so-called self-powered operation, small reverse bias (e.g., -0.1 V) or photovoltaic mode at short-circuit conditions (0 V) has also been employed.^[10,15] Whichever type of operation is used, a low dark current is desirable for a potentially lower noise level and high sensitivity toward weak light signals. Hence, magnitude of the dark current under reverse bias is an

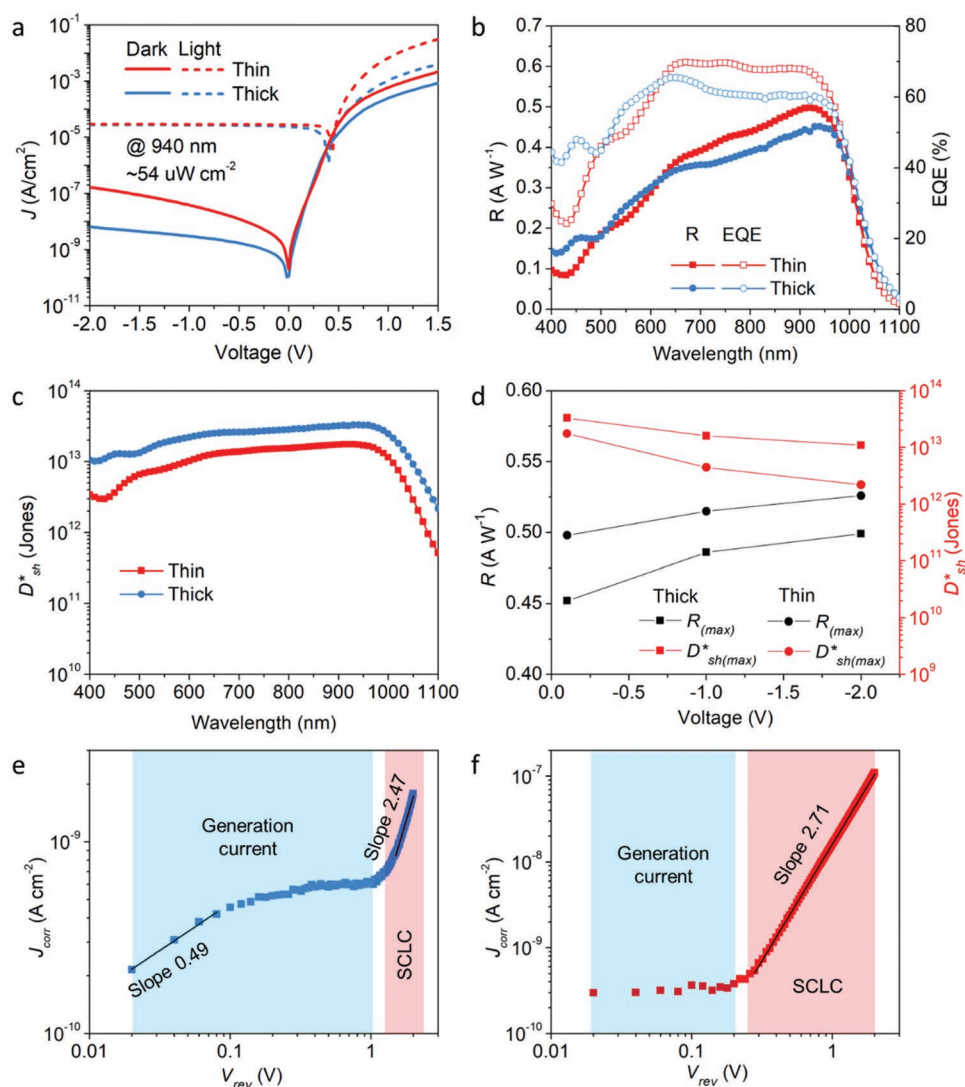


Figure 3. a) J - V curves of the OPDs in the dark and under illumination of NIR. b) Responsivity and EQE, c) shot-noise-limited specific detectivity of the OPDs at -0.1 V. d) Bias-dependent responsivity and shot-noise-limited specific detectivity of the OPDs. e, f) Corrected current density-voltage characteristics of the thick device and thin device under reverse bias.

important parameter for photodetectors. As shown in Figure 3a, the thin device shows a dark current density of 200 nA cm^{-2} at -2 V. The dark current is more effectively suppressed for the thick device, being as low as 7 nA cm^{-2} at -2 V, which is one to four orders of magnitude lower than many of the previously reported OPDs.^[7,9,10,12,18,24–26] Under the illumination of 940 nm monochromatic infrared light of $\approx 54 \mu\text{W cm}^{-2}$, the current density reaches a magnitude of $10^{-5} \text{ A cm}^{-2}$ under reverse bias for both the thin and thick device, promising the high NIR sensitivity of our devices. To evaluate the charge collection efficiency following exciton dissociation, the photocurrent density (J_{ph}) versus effective voltage (V_{eff}) is plotted in Figure S6a (Supporting Information). As the effective voltage increases, the J_{ph} increases as a result of the enhanced charge extraction and decrease of nongeminate losses. The J_{ph} saturates ($J_{ph,sat}$) around 29.3 and $28.2 \mu\text{A cm}^{-2}$ for the thin and thick devices, respectively, which implies similar rate of free charge carrier generation. Charge collection probabilities (P_c), estimated by

the ratio of J_{ph} to $J_{ph,sat}$ (Figure S6b, Supporting Information), are 0.948 and 0.850 for the thin and thick devices under short-circuit condition, respectively. On the one hand, the relatively high values of P_c under short-circuit condition for both types of devices indicate the charge collection efficiency is already quite high without the assistance of an external electric field, a sign of good photon-to-electron conversion for this blend system even with a large thickness. On the other hand, it suggests limited space for further improvement of photoresponse by promoting charge collection with increased reverse bias. In other words, the photodetection limit under the operation condition ($V_{app} \leq 0 \text{ V}$) may be ultimately determined by mainly the electrical characteristics of the photodetectors in the dark. This point will be illustrated in detail later. To further quantify their spectral response, the external quantum efficiency (EQE) was measured as a function of incident light wavelength. For comparison, normal structure devices with the same thin active layer processing condition were also

explored (Figure S7a, Supporting Information). The devices of both structures show similarly shaped EQE profiles. However, the EQE values are overall higher for the inverted one, even compared to the values from the normal structure counterpart under external bias (Figure S7b, Supporting Information). In addition, the dark current under reverse bias is larger by several orders of magnitude due to the inferior charge blocking capability from the poly(3,4-ethylenedioxythiophene) polystyrene sulfonate (PEDOT:PSS) layer and low work function top barium/aluminum electrode (Figure S7c, Supporting Information), which also predicts larger noise signals. Hence, further analysis focuses on the inverted structure OPDs in this work. As shown in Figure 3b, the OPDs show promising EQE values under a small reverse bias of -0.1 V, which vary from 60 to 68% in the NIR wavelength from 750 to 940 nm, with the thin device moderately higher than the thick device. Devices with a medium active layer thickness (≈ 140 nm) were also tested, which show comparable EQE values (Figure S8, Supporting Information). The responsivity (R) of a photodetector is an important figure-of-merit that characterizes the ratio of electrical output to optical input. Quoted in ampere produced per watt of incident light, R can be calculated as follows

$$R = \frac{\text{EQE}}{100\%} \times \frac{\lambda}{1240 (\text{nm W A}^{-1})} \quad (1)$$

where λ is the wavelength of the incident light in nanometer. The spectral profile of responsivity peaks around 920 and 940 nm, reaching 0.50 and 0.45 A W^{-1} for the thin and thick devices, respectively (Figure 3b). With increased reverse bias, the responsivity of the photodetectors is slightly enhanced (Figure S9, Supporting Information), with the highest responsivity reached under -2 V as 0.53 A W^{-1} at 920 nm for the thin device, and 0.50 A W^{-1} at 960 nm for the thick device. To the best of our knowledge, these results present the highest responsivity in the corresponding NIR wavelength range from OPDs without additional gain mechanisms (Figure S10, Supporting Information). The relatively small increase of photoresponse under increased reverse bias (Figure S9, Supporting Information) is also consistent with the high P_C under short-circuit and reverse bias conditions.

In addition to responsivity, the specific detectivity (D^*), quoted in $\text{cm Hz}^{1/2} \text{W}^{-1}$ or Jones, depicts the sensitivity of a photodetector to weak optical signals. It is given by

$$D^* = \frac{R\sqrt{AB}}{i_n} = \frac{R\sqrt{A}}{S_n} \quad (2)$$

where A is the active device area in cm^2 , B is the bandwidth in Hz, i_n is the noise current in A, and S_n is the noise current spectral density in $\text{A Hz}^{-1/2}$. The S_n can be calculated from the current–voltage characteristics in the dark condition with the assumption that the shot noise has a major contribution under reverse bias. Accordingly, the shot-noise-limited specific detectivity (D_{sh}^*) can be obtained

$$D_{\text{sh}}^* = \frac{R\sqrt{A}}{\sqrt{2q i_{\text{d}}}} = \frac{R}{\sqrt{2q J_{\text{d}}}} \quad (3)$$

where i_{d} , J_{d} , and q stand for the dark current, dark current density, and elementary charge, respectively. Contrary to the trend in responsivity, the thick device shows a larger D_{sh}^* compared to the thin device throughout the tested wavelength range due to a smaller dark current (Figure 3c). While both types of devices show large D_{sh}^* over 10^{13} Jones in the NIR wavelength range from 750 to 1000 nm, the thick device also demonstrates $D_{\text{sh}}^* > 10^{13}$ Jones in the visible spectrum as well. It presents one of the highest NIR D_{sh}^* achieved based on organic photodiodes, with a peak D_{sh}^* of 3.31×10^{13} Jones at 940 nm. The D_{sh}^* spectral profiles under different biases are also shown in Figure S11 (Supporting Information). As found, despite having higher responsivity (Figure S9, Supporting Information) under reverse bias for the thin device, the D_{sh}^* under larger reverse biases of -1 and -2 V are still higher for the thick device as a result of a lower dark current and shot noise. It is worth noting that D_{sh}^* monotonically decreases as the reverse bias increases for both devices (Figure 3d and Figure S11, Supporting Information). This again implies that the current characteristics in the dark, rather than the photoresponse performance, pose the limit for the detection, which is similar to the previous work.^[7,23] Nevertheless, even at a relatively large reverse bias of -2 V (corresponding to an electric field strength of 67 kV cm^{-1}), D_{sh}^* maintains over 10^{13} Jones from 860 to 980 nm for the thick device, confirming its robust NIR-sensing capability. To better understand the charge transport and the difference in the dark current between the thin and thick devices, the corrected current density–voltage ($J_{\text{corr}}-V_{\text{rev}}$) characteristics (Figure 3e,f) are analyzed. J_{corr} is calculated according to

$$J_{\text{corr}} = J - \frac{V_{\text{rev}} - JR_s}{R_{\text{sh}}} \quad (4)$$

where J is the absolute value of the apparent current density, V_{rev} is the absolute value of the applied reverse bias, R_s and R_{sh} are the area-normalized series resistance and shunt resistance, respectively, as extracted from the differential resistance.^[27] For the thick device, the region (<0.1 V) where $J_{\text{corr}} \propto V_{\text{rev}}^{0.5}$ corresponds to the charge transport mechanism of generation current.^[28,29] Upon further increasing the reverse bias, $J_{\text{corr}}-V_{\text{rev}}$ curve becomes relatively flat due to the saturated generation current at the fully depleted active layer. Upon further increasing the reverse bias to larger than 1 V, the slope of the logarithmic $J_{\text{corr}}-V_{\text{rev}}$ curve exceeds 2, which is typical of the space charge limited current (SCLC) in the presence of traps.^[30] For the thin device, the active layer is already fully depleted even at very small reverse bias, as can be seen from the flat $J_{\text{corr}}-V_{\text{rev}}$ curve under the reverse bias less than 0.2 V. The onset voltage for the SCLC region is about 0.23 V, much smaller than that of the thick device. In addition to the late onset of SCLC as a result of the injected charges, the thick device also has a larger R_{sh} ($4.4 \times 10^8 \Omega \text{cm}^2$) than that of the thin device ($6.2 \times 10^7 \Omega \text{cm}^2$), as shown in Figure S12 (Supporting Information). The suppressed shunt leakage and SCLC (Figure S13a,b, Supporting Information) make the total dark current in the thick device much smaller and more favorable for high detectivity applications.

The actual noise level was experimentally obtained to avoid performance overestimation.^[31–33] We probed the noise spectral

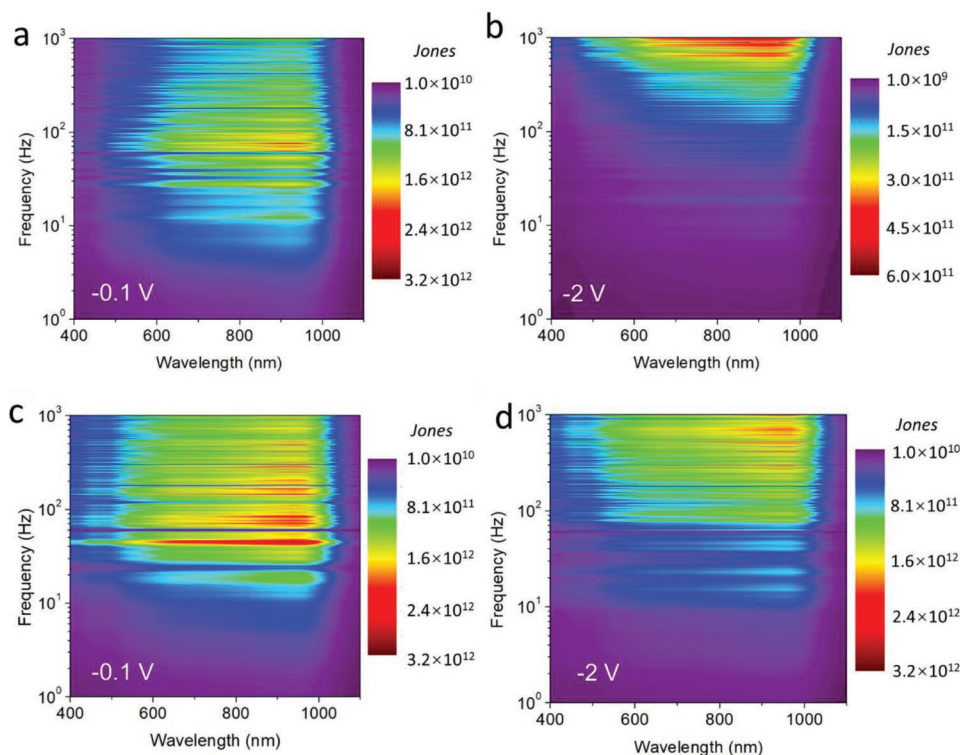


Figure 4. a–d) Specific detectivity (D^*) as a function of frequency and incident light wavelength for the thin device at -0.1 and -2 V (a,b), and for the thick device at -0.1 and -2 V (c,d).

density (S_n) of our OPDs (Figure S14, Supporting Information) with fast Fourier transform of the dark current at -0.1 and -2 V, respectively. At 100 Hz, the S_n is 8.5×10^{-14} and 5.9×10^{-14} A Hz $^{-1/2}$ for the thin and thick devices at -0.1 V, respectively, whereas the values increase to 1.23×10^{-12} and 1.0×10^{-13} A Hz $^{-1/2}$ at -2 V. The noise equivalent power (NEP) stands for the power of the light signal that generates a signal-to-noise (S/N) ratio of unity with output bandwidth of 1 Hz, characterizing the detection limit of the detector. It can be calculated by

$$\text{NEP} = \frac{S_n}{R} \quad (5)$$

At a frequency of 100 Hz, the thick device has an NEP of 1.2×10^{-13} W Hz $^{-1/2}$ at -0.1 V, and still holds as low as 2.0×10^{-13} W Hz $^{-1/2}$ at -2 V, being one of the few reported OPDs that allow NIR detection of sub-picowatt signals according to the experimentally measured noise characteristics.^[18] It is noticeable that at low bias in the low-frequency region (<100 Hz), the large noise may not be necessarily related to the properties of the OPDs (Figure S15, Supporting Information).

With the measured noise spectra, the contour plot of specific detectivity (D^*) can be derived, as shown in Figure 4. At a small bias of -0.1 V, even at a low frequency where flicker noise is significant (10^{-13} – 10^{-12} A Hz $^{-1/2}$, Figure S14a, Supporting Information), the values for D^* in the whole wavelength range (400 to 1100 nm) are over 10^{10} Jones for both devices (Figure 4a,c). In the frequency-independent region, an overall D^* higher than 10^{12} Jones in the NIR range from 750 to 980 nm is achieved for both devices due to their high

responsivity and relatively low noise ($<10^{-13}$ A Hz $^{-1/2}$). At a larger bias of -2 V, the overall enlarged noise level results in a decrease of D^* to below 10^{12} Jones for the thin device. The maximum D^* is around 5×10^{11} Jones, achieved at the highest tested frequency around 1 kHz (Figure 4b) as a result of the widening of the frequency-dependent region of the noise spectrum (Figure S14b, Supporting Information). This widening presents more dominant flicker noise, which is usually believed to originate from trapping and detrapping of carriers.^[34] The result aligns well with the dramatically increased dark current due to the shunt leakage and injected SCLC under large bias, where the trapping and detrapping events become more apparent with large number of carriers being transported. Conversely, the thick device is still able to uphold D^* over 10^{12} Jones in the original wavelength range with suppressed charge transport. This detectivity is higher than the previously reported NIR detectivity achieved with photodetectors based on organic, organic–hybrid perovskite, and inorganic materials,^[7,18,20,35,36] and is close to one of the highest D^* for visible spectrum realized with thick junction strategy.^[22] The performance also competes well with a Si photodiode (Figure S16, Supporting Information). As the bandgap of the photoactive materials becomes narrower, the D^* of nongain photodetectors based on either organic or inorganic semiconductors becomes increasingly sensitive to the noise level due to a larger concentration of thermally excited carriers. Therefore, further improving D^* relies on controlling the testing conditions, such as lowering the temperature.

The linear dynamic range (LDR) describes the range within which the detector output scales linearly with the input signals. Typically, the LDR can be calculated by Equation (6)

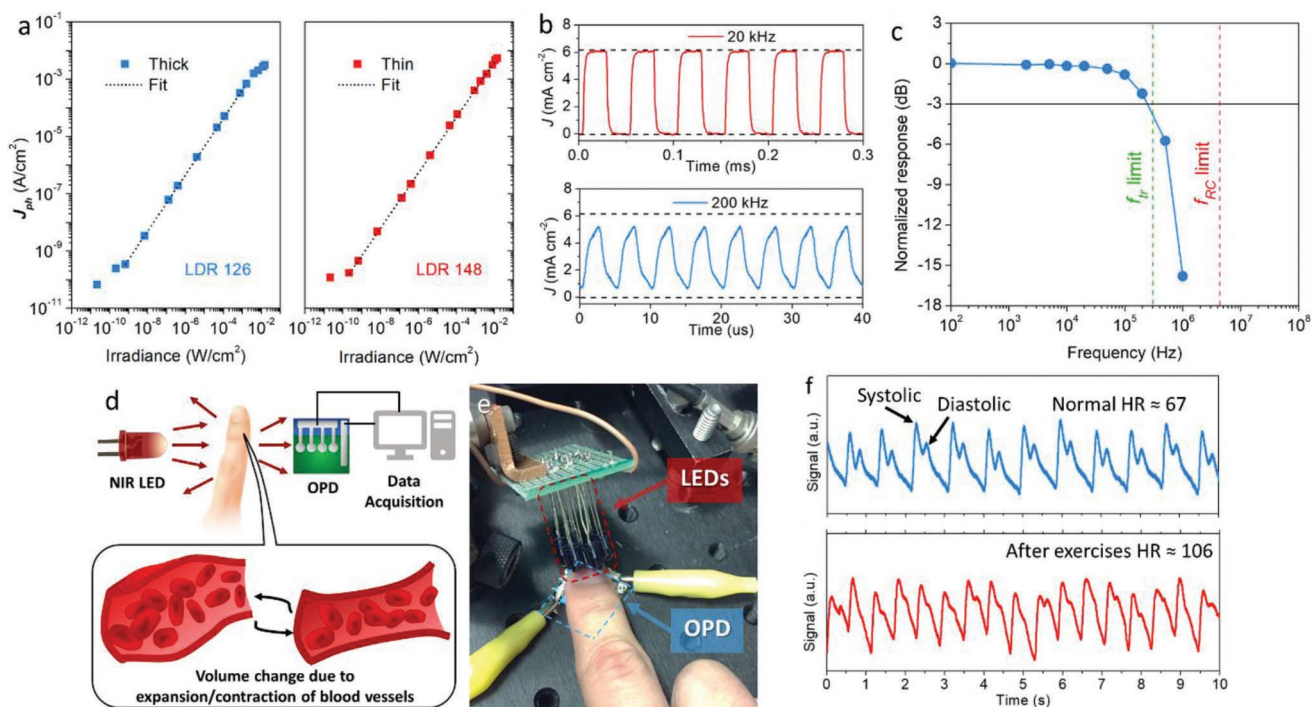


Figure 5. a) Linear dynamic range of the OPDs under illumination of 940 nm LEDs at -0.1 V. b) Phototransient response of the thick device under light modulation frequency of 20 kHz (red) and 200 kHz (blue) at -2 V. c) Normalized response as a function of frequency. The dashed lines indicate the theoretical cutoff frequency limited by transit time (green) and RC time constant (red). d) Working principle of NIR photoplethysmography. e) Setups of HR measurement using the OPD. f) Pulse signal measured from the OPD at normal (upper) and after-exercise (lower) conditions.

$$\text{LDR} = 20 \log \frac{I_{\text{upper}}}{I_{\text{lower}}} = 20 \log \frac{J_{\text{upper}}}{J_{\text{lower}}} \quad (\text{dB}) \quad (6)$$

where I_{upper} and I_{lower} , respectively, stand for the maximum and minimum irradiance beyond or below which the device signal–irradiance relation deviates from linearity. J_{upper} and J_{lower} are the corresponding photocurrent measured at I_{upper} and I_{lower} , respectively. As shown in **Figure 5a**, the photocurrent density (J_{ph}) under irradiation of 940 nm infrared light of different intensity is plotted for the thin and thick devices, which give LDR of 148 and 126 dB, respectively. The saturation (sublinearity) of photocurrent at the higher end of light intensity is usually associated with the effect of bimolecular recombination.^[33] Noticeably, the responsivity at the lowest light intensity is 6.64 and 4.92 A W^{-1} for the thick device and the thin device, respectively. These values correspond to EQE of 876 and 649%, larger than the theoretical limit of 100%. Such superlinearity and EQE greater than 100% suggest that certain gain effect may take place. This can be caused by unbalanced extraction of photogenerated holes or electrons.^[37] Such a “gain” effect has been explored for constructing photomultiplication-type organic photodetectors based on wider bandgap systems.^[38,39] We are currently investigating the possibility of realizing such gain effects under a wider range of light intensity for our narrow-bandgap systems.

To evaluate the response speed of the photodetector, the transient photoresponse behavior of the device was studied. For enhanced charge extraction and fast operation, the photodetectors are usually reversely biased at a relatively large bias. Therefore, the thick device operating under a reverse bias

of -2 V was used for further study due to its better balance between the photoresponse and noise characteristics. **Figure 5b** shows the current density as a function of time for the thick device under 940 nm infrared light modulated at 20 kHz (red) and 200 kHz (blue), respectively. In the former case, the output of the photodetector can follow the on-off switching of the optical signal and reach the steady-state photocurrent and dark current. When illumination modulation is at 200 kHz, the photodetector cannot fully reach the original photocurrent or decay to the dark current due to the limited response speed. An important parameter to evaluate the applicable bandwidth of a photodetector is the cutoff frequency ($f_{3\text{dB}}$), commonly defined as the frequency at which the output of a detector is attenuated to -3 dB, corresponding to 70.8% of the original amplitude. The temporal photoresponse at various light modulation frequencies was recorded to find the corresponding normalized response. As shown in **Figure 5c**, the cutoff frequency is found to be around 240 kHz. In addition, the RC time constant-limited cutoff frequency (f_{RC}) can be calculated by^[40]

$$f_{\text{RC}} = \frac{1}{2\pi RC} \quad (7)$$

where R is the sum of the series resistance (R_{series}) of the device, measured to be 62Ω , and the load resistance of the oscilloscope (50Ω), and C is the junction capacitance of the device, found as 0.34 nF. The corresponding f_{RC} is calculated to be 4.18 MHz. This indicates the limiting factor of the response speed is not the RC time constant but possibly the transit time of the charge

carriers.^[40] The transit time-limited cutoff frequency (f_{tr}) can be obtained as

$$f_{tr} = \frac{3.5}{2\pi\tau_{tr}} = \frac{3.5\mu_{eff}(V + V_{bi})}{2\pi L^2} \quad (8)$$

where τ_{tr} is the transit time of the charge carriers, μ_{eff} is the effective carrier mobility, V is the applied bias, V_{bi} is the built-in voltage, and L is the thickness of the active layer. The mobilities of hole and electron were extracted from the $J^{1/2}$ - V characteristics of the single-carrier diodes (Figure S17, Supporting Information). The μ_{eff} is calculated to be $1.74 \times 10^{-4} \text{ cm}^2 \text{ V}^{-1} \text{ s}^{-1}$, which corresponds to a τ_{tr} of 1.82 μs and a calculated f_{tr} of 306 kHz. This value is fairly close to the experimentally determined value of ≈ 240 kHz. The cutoff frequency is comparable to some other OPDs and is more than enough for applications such as image sensors and medical monitoring.^[2,40]

As a preliminary assessment of the practical application of the NIR OPDs, we carried out a simple photoplethysmography (PPG) test using our OPDs. One of the functions of PPG, a low-cost noninvasive optical technique, is monitoring the pulse and determining the heart rate (HR). The basic working principle is presented in Figure 5d. The light emitted from the LEDs is partially absorbed, reflected, and/or scattered by human tissues, which can be detected by an optical sensor. As a result of the change in blood volume upon each cardiac cycle, the pulsatile (AC) signal which is superimposed with various low-frequency signals, can be extracted to evaluate the heart rate.^[2,41] Figure 5e shows the setups of the HR measurement, which was conducted in the dark to minimize background signal from the surroundings. The HR of one of the authors was measured at their resting and after-exercise conditions, respectively (Figure 5f). In both cases, the typical systolic and diastolic peaks in a PPG profile can be identified. By dividing 60 s by the averaged interbeat interval (IBI) in each case, the HR was determined to be 67 and 106 beats min^{-1} for the author at resting and after-exercise conditions, respectively.

High-performance solution-processed BHJ OPDs based on a new ultranarrow-bandgap nonfullerene acceptor, CO1-4Cl, have been realized for sensitive NIR detection. The present OPDs can achieve a high maximum responsivity over 0.5 A W^{-1} in the NIR region beyond 900 nm, surpassing existing organic photodiodes in a broad NIR spectrum, to the best of our knowledge. In addition to shunt leakage, we have also determined that the space charge limited current also has significant contribution to the dark current. By using the thick junction strategy, the onset of charge injection was effectively postponed and the shunt leakage was also well suppressed, without significantly compromising the photoresponse. As a result, D^* based on experimentally measured noise current retained as high as 10^{12} Jones at 940 nm, which is close to that of a commercial Si photodiode from the visible spectrum up to 1000 nm in the NIR spectrum. With a competent operating bandwidth ($f_{3\text{dB}}$) of 240 kHz and LDR over 120 dB, real-time heart-rate monitoring by PPG was demonstrated with the optimized OPDs, indicating potential of the OPDs for practical implementation as a highly efficient photodetection platform.

Supporting Information

Supporting Information is available from the Wiley Online Library or from the author.

Acknowledgements

This project was supported by the Mitsubishi Chemical Center for Advanced Materials (MC-CAM). J.V. acknowledges primary funding by the Alexander-von-Humboldt Stiftung. J.L. is grateful to the Center for Advanced Soft Electronics under the Global Frontier Research Program of the Ministry of Science, ICT & Future Planning, Korea (Grant Code No. 2011-0031628) for financial support. The GIWAXS measurement used resources of the Advanced Light Source, which is a DOE Office of Science User Facility under Contract No. DE-AC02-05CH11231. The authors are grateful to Dr. Alexander A. Mikhailovsky and Benjamin R. Luginbuhl for assistance with the OPD characterization setups. The PPG was collected from one of the authors under their informed consent. No ethical approval was necessary.

Conflict of Interest

The authors declare no conflict of interest.

Keywords

bulk heterojunctions, high responsivity, near-infrared, organic photodiodes, photodetectors

Received: September 14, 2019

Revised: October 22, 2019

Published online: November 12, 2019

- [1] J. Byrnes, *Unexploded Ordnance Detection and Mitigation*, Springer Science & Business Media, Berlin, Germany **2008**.
- [2] H. Xu, J. Liu, J. Zhang, G. Zhou, N. Luo, N. Zhao, *Adv. Mater.* **2017**, *29*, 1700975.
- [3] M. S. Millán, J. Escofet, *Opt. Lett.* **2004**, *29*, 1440.
- [4] P. Jonsson, J. Casselgren, B. Thörnberg, *IEEE Sens. J.* **2015**, *15*, 1641.
- [5] R. Weissleder, *Nat. Biotechnol.* **2001**, *19*, 316.
- [6] X. Liu, Y. Lin, Y. Liao, J. Wu, Y. Zheng, *J. Mater. Chem. C* **2018**, *6*, 3499.
- [7] Z. Wu, W. Yao, A. E. London, J. D. Azoulay, T. N. Ng, *Adv. Funct. Mater.* **2018**, *28*, 1800391.
- [8] Q. Lin, A. Armin, P. L. Burn, P. Meredith, *Laser Photonics Rev.* **2016**, *10*, 1047.
- [9] Y. Yao, Y. Liang, V. Shrotriya, S. Xiao, L. Yu, Y. Yang, *Adv. Mater.* **2007**, *19*, 3979.
- [10] X. Gong, M. Tong, Y. Xia, W. Cai, J. S. Moon, Y. Cao, G. Yu, C.-L. Shieh, B. Nilsson, A. J. Heeger, *Science* **2009**, *325*, 1665.
- [11] X. Zhou, D. Yang, D. Ma, *Adv. Opt. Mater.* **2015**, *3*, 1570.
- [12] H. Zhang, S. Jenatsch, J. De Jonghe, F. Nüesch, R. Steim, A. C. Véron, R. Hany, *Sci. Rep.* **2015**, *5*, 9439.
- [13] M. Young, J. Suddard-Bangsund, T. J. Patrick, N. Pajares, C. J. Travers, M. C. Barr, S. Y. Lunt, R. R. Lunt, *Adv. Opt. Mater.* **2016**, *4*, 1028.
- [14] M.-S. Choi, S. Chae, H. J. Kim, J.-J. Kim, *ACS Appl. Mater. Interfaces* **2018**, *10*, 25614.
- [15] L. Xiao, S. Chen, X. Chen, X. Peng, Y. Cao, X. Zhu, *J. Mater. Chem. C* **2018**, *6*, 3341.

- [16] H. Yao, Y. Cui, R. Yu, B. Gao, H. Zhang, J. Hou, *Angew. Chem., Int. Ed.* **2017**, *56*, 3045.
- [17] J. Lee, S.-J. Ko, M. Seifrid, H. Lee, B. R. Luginbuhl, A. Karki, M. Ford, K. Rosenthal, K. Cho, T.-Q. Nguyen, G. C. Bazan, *Adv. Energy Mater.* **2018**, *8*, 1801212.
- [18] W. Li, Y. Xu, X. Meng, Z. Xiao, R. Li, L. Jiang, L. Cui, M. Zheng, C. Liu, L. Ding, Q. Lin, *Adv. Funct. Mater.* **2019**, *29*, 1808948.
- [19] G. Wu, R. Fu, J. Chen, W. Yang, J. Ren, X. Guo, Z. Ni, X. Pi, C.-Z. Li, H. Li, H. Chen, *Small* **2018**, *14*, 1802349.
- [20] H. Wang, S. Xing, Y. Zheng, J. Kong, J. Yu, A. D. Taylor, *ACS Appl. Mater. Interfaces* **2018**, *10*, 3856.
- [21] K.-J. Baeg, M. Binda, D. Natali, M. Caironi, Y.-Y. Noh, *Adv. Mater.* **2013**, *25*, 4267.
- [22] A. Armin, M. Hamsch, I. K. Kim, P. L. Burn, P. Meredith, E. B. Namdas, *Laser Photonics Rev.* **2014**, *8*, 924.
- [23] J. Lee, S.-J. Ko, H. Lee, J. Huang, Z. Zhu, M. Seifrid, J. Vollbrecht, V. V. Brus, A. Karki, H. Wang, K. Cho, T.-Q. Nguyen, G. C. Bazan, *ACS Energy Lett.* **2019**, *4*, 1401.
- [24] S. Xiong, J. Tong, L. Mao, Z. Li, F. Qin, F. Jiang, W. Meng, T. Liu, W. Li, Y. Zhou, *J. Mater. Chem. C* **2016**, *4*, 1414.
- [25] X. Hu, Y. Dong, F. Huang, X. Gong, Y. Cao, *J. Phys. Chem. C* **2013**, *117*, 6537.
- [26] J. Qi, L. Ni, D. Yang, X. Zhou, W. Qiao, M. Li, D. Ma, Z. Y. Wang, *J. Mater. Chem. C* **2014**, *2*, 2431.
- [27] C. M. Proctor, T.-Q. Nguyen, *Appl. Phys. Lett.* **2015**, *106*, 083301.
- [28] S. M. Sze, K. K. Ng, *Physics of Semiconductor Devices*, Wiley, New York **2006**.
- [29] V. V. Brus, O. L. Maslyanchuk, M. M. Solovan, P. D. Maryanchuk, I. Fodchuk, V. A. Gnatyuk, N. D. Vakhnyak, S. V. Melnychuk, T. Aoki, *Sci. Rep.* **2019**, *9*, 1065.
- [30] M. A. Lampert, P. Mark, *Current Injection in Solids*, Academic, San Diego, CA, USA **1970**.
- [31] Z. Wu, Y. Zhai, H. Kim, J. D. Azoulay, T. N. Ng, *Acc. Chem. Res.* **2018**, *51*, 3144.
- [32] I. K. Kim, J. H. Jo, J. (B.) Lee, Y. J. Choi, *Org. Electron.* **2018**, *57*, 89.
- [33] Y. Fang, A. Armin, P. Meredith, J. Huang, *Nat. Photonics* **2019**, *13*, 1.
- [34] Y. Fang, J. Huang, *Adv. Mater.* **2015**, *27*, 2804.
- [35] S. Manna, S. Das, S. P. Mondal, R. Singha, S. K. Ray, *J. Phys. Chem. C* **2012**, *116*, 7126.
- [36] J.-Q. Liu, Y. Gao, G.-A. Wu, X.-W. Tong, C. Xie, L.-B. Luo, L. Liang, Y.-C. Wu, *ACS Appl. Mater. Interfaces* **2018**, *10*, 27850.
- [37] J. Miao, F. Zhang, *Laser Photonics Rev.* **2019**, *13*, 1800204.
- [38] J. Miao, F. Zhang, M. Du, W. Wang, Y. Fang, *Adv. Opt. Mater.* **2018**, *6*, 1800001.
- [39] L. Li, F. Zhang, W. Wang, Q. An, J. Wang, Q. Sun, M. Zhang, *ACS Appl. Mater. Interfaces* **2015**, *7*, 5890.
- [40] M. Biele, C. M. Benavides, J. Hürdler, S. F. Tedde, C. J. Brabec, O. Schmidt, *Adv. Mater. Technol.* **2019**, *4*, 1800158.
- [41] J. Allen, *Physiol. Meas.* **2007**, *28*, R1.